Accepted manuscript version
Inorg. Chem. Front., 2025, 12, 2856-2871
DOI for the published journal article (PJA): 10.1039/D4QI03259D

ARTICLE

Determining the Zero-Field Cooling/ Field Cooling Blocking Temperature from *AC*-Susceptibility data for Single-Molecule Magnets

Received 00th January 20xx,
Accepted 00th January 20xx

DOI: 10.1039/x0xx00000x

Yolimar Gil,[a] María Mar Quesada-Moreno,[b*] María A. Palacios,[c] Silvia Gómez-Coca,[d*] Enrique Colacio,[c*] Eliseo Ruiz,[d*] Daniel Aravena,[e*]

We present a general relation between the magnetisation blocking temperature (T_B) measured using the zero-field cooling/field cooling technique (ZFC/FC) and their temperature-dependent spin relaxation time obtained from ac-susceptibility and magnetisation decay measurements. The presented mathematical approach provides ZFC/FC blocking temperatures at any heating rate (R_H), providing comparable values to those obtained experimentally, as demonstrated by testing 106 examples for reported single-molecule magnets (SMMs) where the ZFC/FC curve was measured. This procedure is examined in further detail for a new single-molecule magnet $[Dy(OPAd_2Bz)_2(H_2O)_4Br]Br_2{\cdot}4THF$ (**1**) ($OPAd_2Bz$: di(1-adamantyl)benzylphosphine oxide). For this compound, ZFC/FC measurements were made at a broad range of heating rates (0.01 K/min - 5 K/min), which agreed with the general behaviour predicted from ac-susceptibility data. We discuss how the demagnetisation mechanism determines the sensitivity of T_B with respect to the heating rate: T_B is mostly insensitive to R_H for Orbach relaxation, while there is a larger sensitivity for Raman-limited systems. Our conclusions provide a clear physical interpretation of ZFC/FC blocking temperatures, aiding in the proper contextualization of this figure of merit.

Introduction

In the early 1990s, the discovery of Single Molecule Magnets (SMMs) sparked a revolution in the field of molecular magnetism. These molecular transition metal coordination compounds exhibit a magnetic memory effect, which arises from the blocking magnetisation via an anisotropy barrier (U_{eff}) for prolonged periods in the absence of an external magnetic field and below a critical temperature known as the blocking temperature (T_B).[1-5] SMMs have garnered extensive investigation due to their immense technological potential in molecular spintronics, ultra-high-density data storage, and quantum information technologies using spin qubits.[6-11, 12,]

However, a significant challenge in the field remains, necessitating the achievement of a magnetic memory effect at practical/high temperatures while maintaining high thermal stability in the presence of air and humidity.[13, 14] Among the promising candidates, mononuclear SMM complexes containing a single magnetic ion represent the smallest nanomagnets with modulable magnetic anisotropy achieved through precise control of the electronic structure, involving the selection of metal ions and ligands.[15-26] Notably, the Dy^{III} ion, with its unquenched orbital momentum and large magnetic anisotropy, has emerged as a leading candidate to revolutionize technology based on electron spin.[15-20, 27-29]

Experimental and computational studies have revealed that strong axial crystal fields, achieved through axial distribution of ligands, are crucial for Dy^{III} complexes to exhibit remarkable SMM behaviour.[15-20,30-32] More recent approaches seek for the attenuation of vibrational displacements to hamper Raman relaxation.[33, 34] For future systems, some theoretical works suggest exploring surface deposition of SMMs[35] and higher oxidation states[36] in case of lanthanide complexes. In the quest to develop practical SMM applications, reaching a blocking temperature (T_B) above liquid nitrogen temperature (77 K) is crucial. The Dy^{III} mononuclear $[Dy(C_5Me_5(Cp^{iPr5})][B(C_6F_5)_4]$ [37] and the mixed-valence $Dy^{III}Dy^{II}$ dinuclear $[Dy_2I_3(Cp^{iPr5})_2]$ metallocene[38] compounds have achieved a landmark performance with U_{eff} = 2217 K and 2347 K, respectively, and T_B = 80 K in both cases, surpassing this crucial barrier. The

[a] *Facultad de Ciencias Químicas y Farmacéuticas, Universidad de Chile, Casilla 233, Santiago, Chile.*
[b] *Departamento de Química Física y Analítica, Universidad de Jaén, Campus Las Lagunillas, 23071, Jaén, Spain. email: mqmoreno@ujaen.es*
[c] *Departamento de Química Inorgánica, Facultad de Ciencias, Universidad de Granada, 18071Granada, Spain. email: ecolacio@ugr.es*
[d] *Departament de Química Inorgànica i Orgànica and Institut de Recerca de Química Teòrica i Computacional, Universitat de Barcelona, Diagonal 645, 08028 Barcelona, Spain. email: silvia.gomez.coca@ub.edu, eliseo.ruiz@qi.ub.edu*
[e] *Departamento de Química de los Materiales, Facultad de Química y Biología, Universidad de Santiago de Chile, Casilla 40, Correo 33, Santiago, Chile. email: daniel.aravena.p@usach.cl*
† Footnotes relating to the title and/or authors should appear here.
Supplementary Information available: [details of any supplementary information available should be included here]. See DOI: 10.1039/x0xx00000x

uniaxial local symmetry stabilizes the largest m_J = ±15/2 ground state, [39, 40] in the former, and the collinearity of the local anisotropy axes and the strong 4f-radical coupling in the latter, resulting in significant separation from the first and higher excited states.[38, 41, 42] However, compounds with such low coordination are unstable and the need for more stable systems with similar magnetic properties arises. Different high-order symmetry axes, such as trigonal bipyramidal (D_{3h}), [43, 44] square antiprismatic (D_{4d}),[45-49] sandwich,[37, 50-54] and pentagonal bipyramidal (D_{5h}),[55-73] have been recommended to favour slower relaxation of magnetisation by reducing transverse anisotropy and suppressing Quantum Tunnelling of the Magnetisation (QTM). The presence of a high-order symmetry axis also promotes the collinearity of anisotropic axes of the excited and ground states, leading to larger U_{eff} values.[74, 75] Nonetheless, it is essential to engineer molecular vibrations to control the spin lifetime of SMM complexes,[76] as flexible lattices are responsible for fast relaxation. Addressing the requirements of high-temperature performance and thermal air and humidity stability, mononuclear Dy^{III} SMMs with D_{5h} geometry hold a fair position, displaying in many cases stability against these factors with U_{eff} and T_B value as high as 1162 K [63] and 36 K,[70] respectively. Although some recent mononuclear Dy^{III} SMMs with D_{5h} geometry have been shown to be air-sensitive, the majority are stable.[60, 61, 73, 77] Recently, the role of the spin-vibrational coupling in designing high-performance pentagonal bipyramidal Dy^{III} SMMs has been unravelled using a combination of Density Functional Theory (DFT) and Complete Active Space Self- Consistent Field (CASSCF) calculations.[33] There are about thirty examples of mononuclear Dy^{III} SMMs with D_{5h} geometry, but those employing axial bulky phosphine oxide type ligands (high electron density) and weak donor equatorial ones (e.g., water),[56-59, 62, 64] are relatively scarce. These D_{5h} based SMMs represent a highly efficient approach to constructing new high-performance SMMs.

As mentioned previously, the Dy^{III} metallocene compounds $[Dy(C_5Me_5(Cp^{iPr5})][B(C_6F_5)_4]$ and $[Dy_2I_3(Cp^{iPr5})_2]$ show the highest blocking temperature reported to date. This value was measured by the maximum temperature at which magnetic hysteresis is observed (herein $T_{B\text{-}H}$). However, there are two other ways to quantify the blocking temperature: the temperature at which the magnetic relaxation time is equal to 100 seconds ($T_{B\text{-}100}$) and the maximum in the zero-field cooled (ZFC) magnetic susceptibility ($T_{B\text{-}ZFC}$). For the dysprosium metallocene cation, these values are 67 and 52 K, respectively. This example remarks how different the blocking temperature can be depending on the measurement technique. Furthermore, key experimental parameters can also influence T_B significantly. In the case of magnetic hysteresis measurements, $T_{B\text{-}H}$ varies by the field sweep rate, where faster sweep rate programs lead to higher blocking temperatures. Focusing on ZFC/FC experiments, $T_{B\text{-}ZFC}$ is sensitive to the heating rate, with faster heating rates leading to higher blocking temperatures. Unfortunately, the experimentally employed heating rate is often missing in literature reports, hindering a rigorous comparison between systems from different publications. Another issue is related to the misunderstanding of $T_{B\text{-}ZFC}$ definition, since some authors refer to this value as the temperature where ZFC and FC curves diverge, which corresponds to the irreversibility temperature (T_{irrev}), which is higher than that of $T_{B\text{-}ZFC}$.[78] Although $T_{B\text{-}100}$ usually does not depend strongly on the measurement conditions, the 100 seconds definition is arbitrary and it is not clear why the blocking temperature at this specific relaxation time is more informative of SMM behaviour than other thresholds. Blocking temperatures are convenient as "single-molecule magnet" performance metrics since they condense a complex magnetic relaxation dependence in a single figure. Moreover, the existence of a magnetic blocking temperature provides a clear definition of a "molecular magnet" which goes beyond the presence of slow relaxation of the magnetisation. However, other demagnetisation parameters as magnetic coercivities and parameters such as demagnetisation barriers (U_{eff}) are also relevant for the assessment of SMM performance.

In this paper, we propose a new approach to estimate $T_{B\text{-}ZFC}$ at any heating rate from the temperature-dependent spin relaxation time obtained from ac-susceptibility and magnetisation decay measurements, to advance towards a more harmonized definition of T_B. In this way, $T_{B\text{-}ZFC}$ data from different studies can be better compared, as many literature examples of ZFC/FC experiments do not inform the heating rate. Furthermore, the model allows for the estimation of $T_{B\text{-}ZFC}$ in cases where the ZFC/FC experiment was not done. Experimentally, performing the ZFC/FC experiment together with AC-magnetometry measurements is not a practical problem, so the main use of our proposed method is not to avoid the ZFC/FC experiment but to provide a new tool to contextualize and estimate ZFC/FC blocking temperatures.

To validate this new model, we have compared $T_{B\text{-}ZFC}$ values for 106 literature examples of SMMs that have reported with the ZFC/FC data, including both lanthanide and transition metal systems. Furthermore, we conducted a detailed ac-susceptibility and ZFC/FC study for a new Dy^{III} SMM with D_{5h} geometry. Concretely, we measured ZFC/FC curves for a wide range of heating rates, demonstrating that the presented model is accurate in predicting $T_{B\text{-}ZFC}$ values and captures the heat rate dependence of the blocking temperature.

Results and Discussion

Mathematical Model for ZFC/FC Blocking Temperature determined from AC Susceptibility

Our first goal is relating the blocking temperature measured by zero field cooling experiments with an expression in terms of the temperature dependent relaxation time. Experimentally, susceptibility is calculated as the ratio between the magnetic moment and the applied magnetic field. The isothermal (static) susceptibility is:

$$\chi_T = \frac{M_{eq}}{B} = \frac{gS(P_\uparrow - P_\downarrow)_{eq}}{B} \quad (1)$$

Where M_{eq} is the magnetic moment corresponding to equilibrium population at a given temperature and magnetic field (B), g is the Landé factor, S is the spin and $P_\uparrow - P_\downarrow$ is the population difference between spin up and down species. The expression for the non-equilibrium susceptibility measured in the ZFC experiment is analogous to Eq. 1 when the magnetic moment $P_\uparrow - P_\downarrow$ term is out of equilibrium.

Combining the equilibrium and out of equilibrium expressions for magnetic susceptibility, χ_{ZFC} is defined as:

$$\chi_{ZFC} = \frac{(P_\uparrow - P_\downarrow)}{(P_\uparrow - P_\downarrow)_{eq}}\,\chi_T = \chi_T\left[\frac{(P_\uparrow - P_\downarrow) - (P_\uparrow - P_\downarrow)_{eq}}{(P_\uparrow - P_\downarrow)_{eq}} + 1\right] = \chi_T\left[\frac{\Delta M}{(P_\uparrow - P_\downarrow)_{eq}} + 1\right] \quad (2)$$

The numerator in the r.h.s of Eq. 2 is the difference between the equilibrium and out of equilibrium magnetic moments (ΔM). The kinetic equation for a system after a perturbation is:

$$\frac{d\Delta M}{dt} = -\tau^{-1}(\mathrm{T})\Delta M \quad (3)$$

Where the relaxation rate τ^{-1} is temperature dependent. In the ZFC experiment, the sample is initially cooled in absence of an external direct magnetic field. After reaching a cryogenic temperature, the magnetic moment is measured using a small magnetic field and the sample is heated at a rate $R_H\ (K/s)$:
Hence, Eq. 3 becomes:

$$\frac{d\Delta M}{dT} = -\tau^{-1}(\mathrm{T})\Delta M/R_H \quad (4)$$

The general solution of Eq. 4 is:

$$\Delta M = C_1 \exp\left(-R_H^{-1}\int \tau^{-1}dT\right) \quad (5)$$

where C_1 is the magnetisation at the beginning of the ZFC heating step, if all spins remain frozen when the magnetic field needed for the measurement of the heating curve is turned on, $C_1 = -\tanh\left(-\frac{\beta g S B}{T}\right)$ and the combination of Eqs. 2 and 5 yields the simple form:

$$\chi_{ZFC} = \chi_T\left[-\exp\left(-R_H^{-1}\int \tau^{-1}dT\right) + 1\right] \quad (6)$$

In practice, the magnetic moment is not zero at the beginning of the heating step. This is the typical situation in ZFC/FC experiments and depends on the orientational distribution of magnetic moments, their alignment with respect to the external field and operational parameters, as the time needed to stabilize the initial temperature on each experiment. Since this parameter is sample and experiment dependent, we assume it as an effective constant C_1', with a value between 0 and 1. In this way, Eq. 7 becomes:

$$\chi_{ZFC} = \chi_T\left[-\mathrm{C}_1'\exp\left(-R_H^{-1}\int \tau^{-1}dT\right) + 1\right] = \lambda\chi_T \quad (7)$$

Where term in parenthesis is the fraction of relaxed magnetic moments ($0 \le \lambda \le 1$). Eq. 7 allows for the determination of the blocking temperature by the evaluation of the maximum of χ_{ZFC} for an arbitrary χ_T. Importantly, Eq. 7 can be applied to different experimental conditions (such as the presence of magnetic fields) if these effects are present in the data that produced the τ^{-1} function. Although all results from this paper can be obtained by the former equation, we are also interested in an analytical expression for T_B. Thus, the maximum of χ_{ZFC} is expressed as:

$$\frac{d\chi_{ZFC}}{dT}(T_B) = 0 = \frac{d\chi_T}{dT} - \frac{d\chi_T}{dT}\mathrm{C}_1'\exp\left(-R_H^{-1}\int_0^{T_B}\tau^{-1}dT\right) + \chi_T R_H^{-1}\tau^{-1}(T_B)\mathrm{C}_1'\exp\left(-R_H^{-1}\int_0^{T_B}\tau^{-1}dt\right) \quad (8)$$

$$\chi_T R_H^{-1}\tau^{-1}(T_B)\,\mathrm{C}_1'\exp\left(-R_H^{-1}\int_0^{T_B}\tau^{-1}dT\right) = \frac{d\chi_T}{dt}\left[-1 + \mathrm{C}_1'\exp\left(-R_H^{-1}\int_0^{T_B}\tau^{-1}dT\right)\right] \quad (9)$$

$$\chi_T/\frac{d\chi_T}{dt} = \frac{R_H\left[-1+\mathrm{C}_1'\exp\left(-R_H^{-1}\int_0^{T_B}\tau^{-1}dT\right)\right]}{\left[\tau^{-1}(T_B)\,\mathrm{C}_1'\exp\left(-R_H^{-1}\int_0^{T_B}\tau^{-1}dT\right)\right]} \quad (10)$$

For simplicity, we consider that the isothermal susceptibility reasonably follows the Curie law:

$$\chi_T/\frac{d\chi_T}{dt} = -T_B \quad (11)$$

The assumption of Curie law greatly simplifies the following equations but can be reversed if needed.
Hence, the blocking temperature is:

$$T_B = \frac{\mathrm{R_H}\left[1 - \mathrm{C}_1'\exp\left(-R_H^{-1}\int_0^{T_B}\tau^{-1}dT\right)\right]}{\mathrm{C}_1'\exp\left(-R_H^{-1}\int_0^{T_B}\tau^{-1}dT\right)\tau^{-1}(T_B)} \quad (12)$$

Eq. 12 can be expressed in a way that the l.h.s coincides with the term in square brackets from Eq. 7:

$$1 - \mathrm{C}_1'\exp\left(-R_H^{-1}\int_0^{T_B}\tau^{-1}dT\right) = \frac{T_B}{T_B + \mathrm{R_H}\tau(T_B)} \quad (13)$$

Thus, the blocking temperature can be estimated knowing the heating rate, the temperature dependence of τ and C_1'. In sum, T_B can be either obtained by Eqs. 7 or 12, where the latter expression gives an explicit term for T_B by assuming the Curie law. We analysed how these two approaches perform for a selected group of experimental literature examples (see Section 3 and Table S7 in ESI) and concluded that both equations provide satisfactory results for T_B, especially for larger values of C_1'. In general, the Curie Law assumption from Eq. 13 gives slightly lower calculated T_B values than Eq. 7, which employs the experimental dependence of χ. In conclusion, we recommend employing any of the two equations with $\mathrm{C}_1' = 1$ to obtain reliable estimations for $T_{B-ZFC/FC}$.

Synthesis and Characterization of the Dy^{III} SMM with D_{5h} symmetry

In view of the previous considerations, we focused our efforts on the preparation of a mononuclear Dy^{III} coordination complex $[Dy(OPAd_2Bz)_2(H_2O)_4Br]Br_2{\cdot}4THF$ (**1**) ($OPAd_2Bz$: di(1-adamantyl)benzylphosphine oxide) close to ideal pentagonal bipyramidal geometry, which fulfils all the desired characteristics to obtain SMMs with high U_{eff} and T_B, that is, strong axial crystal field, humidity and air stability, and rigid networks to avoid rapid relaxation. A strong axial crystal field is created by the two bulky di(1-adamantyl)benzylphosphine oxide ligands located in axial positions, which lead to magnetic hysteresis that remains open up to 14 K, one of highest values for air/humidity stable SMMs synthesized to date. Four water molecules and one bromide anion are located in equatorial positions, which is a structural difference with respect to previous compounds with axial phosphine oxide ligands, where five water molecules are located instead.[56-59, 62] Furthermore, we will provide detailed insight into the mechanism that governs the magnetic relaxation of complex **1** by using *ab initio* CASSCF based computational methods.

Complex **1** was prepared by the solvothermal reaction of the ligand di(1-adamantyl)benzylphosphine oxide with anhydrous $DyBr_3$ in anhydrous tetrahydrofuran and in 2:1 molar ratio using a 15 ml Teflon-lined stainless container and keeping it at 100 °C for three days (see ESI for further details). The resulting solution from the solvothermal reaction was allowed to evaporate at room temperature for several days, whereupon large colourless prismatic single-crystals of $[Dy(OPAd_2Bz)_2(H_2O)_4Br]Br_2{\cdot}4THF$ (**1**) were obtained, which are air-stable (Fig. 1).

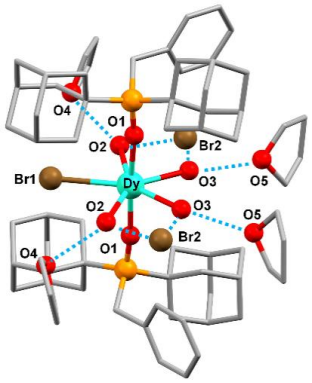

Figure 1. Perspective view of the molecular structure of $[Dy(OPAd_2Bz)_2(H_2O)_4Br]Br_2{\cdot}4THF$ (**1**). Code colours: dysprosium (cyan), oxygen (red), bromide (brown), phosphorus (orange), and carbon (grey). Hydrogen atoms are omitted for clarity. Blue dashed lines indicate hydrogen bond interactions.

The molecular structure of **1** consists of $[Dy(OPAd_2Bz)_2(H_2O)_4Br]^{2+}$ cationic units, with its charge balanced by two free bromide anions, and four crystallization THF molecules (Fig. 1). The two latter interact with the cationic unit *via* hydrogen bonds. Within the cationic unit, the seven-coordinate Dy^{III} centre exhibits a pentagonal bipyramidal geometry (PBPY-7), very close to an ideal D_{5h} polyhedron, as supported by the continuous shape measures analysis, [79] which provides a S(PBPY-7) value of 0.948 (where 0 corresponds to the ideal D_{5h} geometry) (Table S1, ESI). Two bulky $OPAd_2Bz$ ligands occupy the axial positions, whereas four water molecules and one bromide ion are in the equatorial plane (Fig. 1). The axial Dy–O1 distances (2.210(3) Å) are shorter than the equatorial Dy–O2/O3 (average value of 2.365 Å) and Dy-Br1 (2.8860(6) Å) ones, which indicates that the cationic unit shows a compressed PBPY-7 geometry with an almost linear axial O1–Dy–O1 angle (176.73(16)°) and equatorial Br1–Dy–O2, O2–Dy–O3 and O3–Dy–O3 angles of 74.24(9)°, 71.88(13)° and 68.12(17)°, respectively, close to the ideal angle of 72° (Table S3, ESI). The coordinated bromide atom seems to generate certain steric repulsion with the water molecules close to it, which is reflected in a Br1–Dy–O2 angle greater than 72°. In turn, this brings about the closeness between these two water molecules with the other two, thus showing O2–Dy–O3 and O3–Dy–O3 angles less than 72°. The P–O1–Dy angle is also very close to linearity (173.67(19)°) and the angles between the equatorial and axial atoms are around 90° (Table S3, ESI). Specifically, the local symmetry of the DyO_6Br coordination sphere is C_{2v}, with the C_2 axis lying along the line connecting the coordinated bromide anion and the Dy^{III} ion (Fig. 1). Each coordinated water molecule interacts with one free bromide anion and one THF molecule *via* hydrogen bonds. The O2···Br2 and O3···Br2 donor-acceptor distances show respective values of 3.161(4) Å and 3.154(3) Å, whereas those for the O2···O4(THF) and O3···O5(THF) donor-acceptor distances are 2.802(6) Å and 2.774(19) Å, respectively. Moreover, the shortest Dy···Dy intermolecular distance for **1** is 12.1090(3) Å, which indicates that the $[Dy(OPAd_2Bz)_2(H_2O)_4Br]^{2+}$ units are well separated in the structure. There are no π···π stacking interactions between the aromatic benzene rings of different units. The free bromide atoms establish van der Waals interactions with the benzene hydrogens inside the same unit (3.0386(5) Å), and with the hydrogens of the CH_2 (2.6475(5) Å) and adamantyl groups (2.7673(5) Å) of adjacent units (Figure S3).

Magnetic measurements

The DC magnetic properties of **1** were studied in the 2-300 K temperature range under an applied magnetic field of 0.5 T and the magnetisation was studied in the field range 0 to 7 T at temperatures between 2 and 7 K, see Figure S4. It is worth remarking that the obtained curves clearly show the typical features of magnetisation blocking in an efficient mononuclear Dy^{III}-SMM (deep decrease of $\chi_M T$ at low temperature, sinusoidal behaviour of the magnetisation at low field, divergence between FC and ZFC magnetic susceptibilities at low temperature, and magnetic hysteresis, see below and Figures S4-S11).

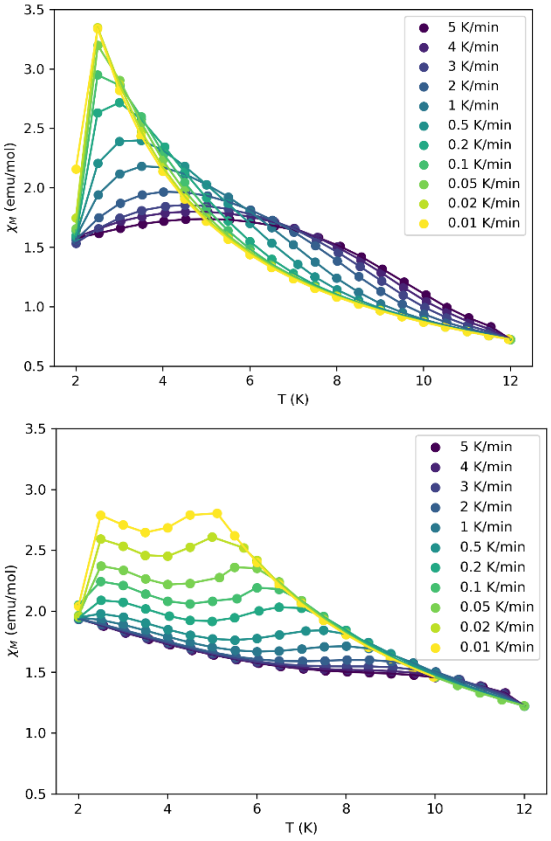

Figure 2. Temperature dependence of χ_M at ZFC conditions at different heating rates and with an applied field of 50 Oe (above) and 500 Oe (below). FC data are omitted for a better appreciation of the ZFC curves. ZFC/FC curves for all data are available as Electronic Supporting Information (Figures S5-S6).

The ZFC/FC magnetic susceptibilities were collected at two magnetic fields and with a wide range of heating rates to evaluate T_B and compare with the proposed model (see Figure 2). For the small field, 50 Oe, at very low heating rates, the ZFC/FC opens slightly at very low temperatures. When increasing the heating rate,

the ZFC and FC curves differ more and the temperatures at which the curves diverge rise to larger values. The maximum of the ZFC curve signalling T_B goes from 2.5 K at 0.01 K/min to 5 K at 5 K/min (Table S4). When increasing the field to 500 Oe, the blocking temperatures rise significantly, which is probably due to the suppression of the relaxation through QTM. At very low heating rates (0.01 K/min), the blocking temperature is around 5K and reaches 8K at 2 K/min. Faster heating rates did not provide values for the blocking temperature since the ZFC curve had no clear maximum (see Figure 2).

Alternating current (AC) magnetic susceptibility measurements were performed to study the slow relaxation of the magnetisation. To obtain the maximum number of relaxation times and be able to study a larger temperature range, two equipment were employed to study the 1-10000 Hz frequency range, a SQUID MPMS XL and a PPMS-9, (see details in the ESI). At zero external DC field, the in-phase (χ_M') and out-of-phase (χ_M'') components of the AC susceptibility show frequency-dependent peaks (Figures S8 and S9) with well-defined maxima in the χ_M'' vs. T plot in the 20 K – 40 K range for higher frequencies (Figure S9), indicating a high magnetisation reversal barrier. The χ_M'' vs. frequency plot displays temperature-dependent maxima in the 19–27 K range (Figure S10). The relaxation times were extracted from fitting of frequency dependence of χ_M'' at different temperatures using the generalized Debye model. The extracted relaxation times are collected in Table S6.

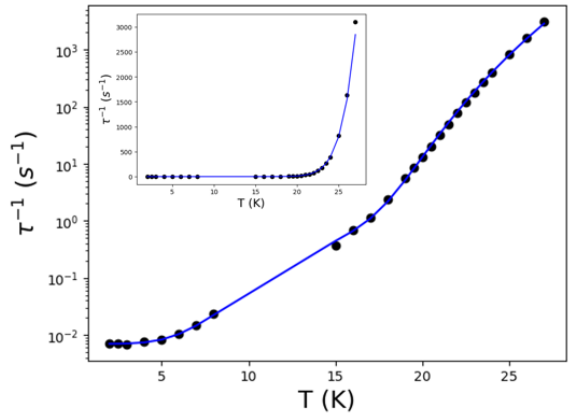

Figure 3. Plot of $\ln(\tau^{-1})$ vs temperature for **1** (in the inset, τ^{-1} vs temperature as in Eq. 14). The values at lower temperatures correspond to the obtained from the magnetisation decay and the values at higher temperatures are the ones derived from the fit of the AC susceptibility data to a generalized Debye function. The blue line corresponds to the fit of the data with Eq. 14.

Magnetisation decay experiments were performed to evaluate relaxation times at lower temperatures. An exponential decay of the magnetisation was clearly observed until 8 K. The obtained data was fit using a stretched exponential function (Figure S7) which is commonly employed in the obtention of relaxation times from magnetisation decay measurements. [80, 81] The obtained τ values are collected on Table S5 and represented in Figure 3 as the $\ln(\tau^{-1})$ vs temperature together with the obtained values from the AC susceptibility measurements. At very low temperature, there is a constant region indicative of quantum tunnelling relaxation. The onset of the Raman regime is discernible from magnetisation decay data, which trend matches with the lowest points measured by ac-susceptibility. The transition between Raman and Orbach demagnetisation is clearly visible around 18K. As the three magnetic relaxation mechanisms are identified in the τ^{-1}(T) curve, the following equation was employed:

$$\tau^{-1} = \tau_{QTM}^{-1} + CT^n + \tau_0^{-1} e^{U_{eff}/kT} \quad (14)$$

Where the effective demagnetisation barrier was adjusted to a value of 427.7 K (297.3 cm^{-1}), with a preexponential factor τ_0 of 4.66 x 10^{-11} s. Raman and tunnelling were fitted to C = 2.64 x 10^{-7} $K^{-n}s^{-1}$, n = 5.28 and τ_{QTM} = 142.7 s, respectively.

For completeness, the field dependent magnetisation measurements at different temperatures were acquired (Figure 4), with a sweep rate of 20 mT s^{-1}. Compound **1** shows clear magnetic hysteresis which remains open up to 14 K, which is one of highest values for air/humidity stable SMMs synthesized to date. The butterfly shape of the hysteresis loop arises from a faster relaxation around zero field and a slower relaxation at intermediate fields. This compound retains a large magnetisation that falls only when H < 20 mT, which can be attributed to the unsuppressed Quantum Tunnelling of the Magnetisation due to symmetry deviation, hyperfine and dipole interactions. When the temperature increases, the hysteresis loop narrows as the relaxation speeds up and results in smaller coercive fields and remanent magnetisation. The hysteresis loop shows a coercive field of 1 T and a remanent magnetisation of 2 □B at 3 K at a sweep rate of 20 mT s^{-1},

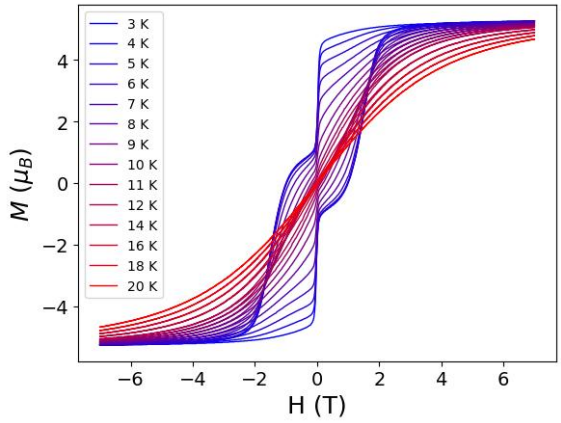

Figure 4. Magnetic hysteresis measurements/hysteresis plot for **1** with a sweep rate of 20 mT s^{-1}.

Ab initio calculations

Ab initio calculations based on the experimental X-ray structural data were performed to provide insight into the mechanism that governs the magnetic relaxation of complex **1**. In particular, multiconfigurational CASSCF calculations implemented in ORCA 5.0.3 program package [82-84]and the CASSCF/RASSI-SO/SINGLE_ANISO approach using OpenMOLCAS[85-87] were carried out. Both programs agree in the general description of the double well potential associated with the ground $^6H_{15/2}$ multiplet. To avoid redundancy in the discussion, we present the ORCA results in the manuscript while OpenMOLCAS data are presented in the Electronic Supporting information for comparison. These methodologies are quite helpful to elucidate and predict the electronic structure and relaxation mechanism of single-molecule magnet complexes.

The computed eight Kramers' doublets (KDs) for **1**, corresponding to the $^6H_{15/2}$ ground state of the Dy^{III} ion, span an energy range of

about 674 cm^{-1} (Electronic Supporting Information, Table S8). The computed temperature dependence of $\chi_M T$ reproduces rather well the experimental temperature dependence of $\chi_M T$ (Figure S4, ESI). The ground KD (KD1) is a pure m_J = |±15/2⟩ state that is highly anisotropic (g_{zz} = 19.86) with negligible transverse components ($g_{xx} \sim g_{yy} < 1.10^{-3}$), establishing thus a strong magnetic anisotropy axis. These *g*-values suggest strongly suppressed QTM within the ground KD (Figure 5), which is consistent with the relatively large experimental value for τ_{QTM} (142.7 s). The anisotropy g_{zz} axis is almost collinear with the pseudo-C_5 axis lying along the axial O–Dy–O bonds (the deviation between the g_{zz} axis and O–Dy–O direction is 1.5°, see Figure S13 and Figure 5 bottom). This strong uniaxial magnetic anisotropy is consistent with the weak ligand field from aqua and bromine ligands in the equatorial plane and the strong donor ligands in the axial positions.

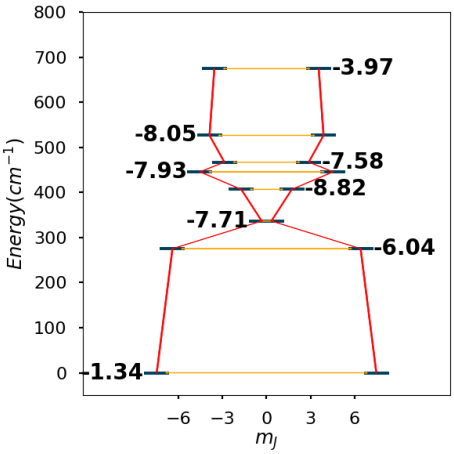

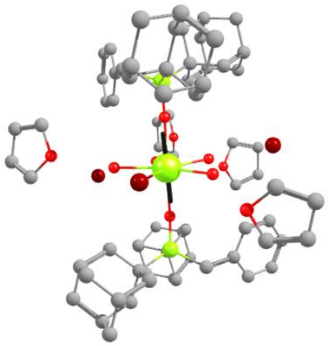

Figure 5. (top) *Ab initio* magnetisation blocking barrier for **1**, where the Kramers' doublets (KDs) are represented as dark blue bars and tunnelling relaxation times (τ_{QTM}) between the connecting pairs are indicated as orange lines and the values are represented in log 10 scale. (bottom) Molecular structure for **1** with the calculated orientation of the main magnetic axis of the ground Kramers' doublet (KD1) (black line). Colour code: Dy(green), O(red), P(orange), Br(brown) and C(grey).

The first excited state (KD2) lies at 275.2 cm^{-1} above the ground state. This KD2 is also axial in nature, with g_{zz} = 16.92, g_{xx} = 0.13, and g_{yy} = 0.27. In this case, the g_z tensor passes through the O–Dy–O direction again and presents a deviation of 6.4° with respect to the g_{zz} anisotropy axis of the ground state. The transverse components of KD2 can be large enough to promote magnetic relaxation via the first excited state, giving a calculated magnetisation barrier U_{cal} of 275.2 cm^{-1} (396 K), which is close to the experimental energy barrier U_{eff} of 427.7 K. The next excited state (KD3) is close in energy (336.6 cm^{-1}, 484 K) and shows large transverse components of *g* (g_{xx} = 0.42 and g_{yy} = 1.63). Tunnelling relaxation times were calculated according to an *ab initio* model based on spin-dipolar interaction.[88] For the ground state (KD1) the calculated tunnelling time is 4.6×10^{-2} s while for the first excited state (KD2) it is much faster (9.1×10^{-7} s), which is consistent with the large transverse *g*-tensors obtained for this latter, confirming that the magnetic relaxation for **1** occurs via the first excited state (KD2).

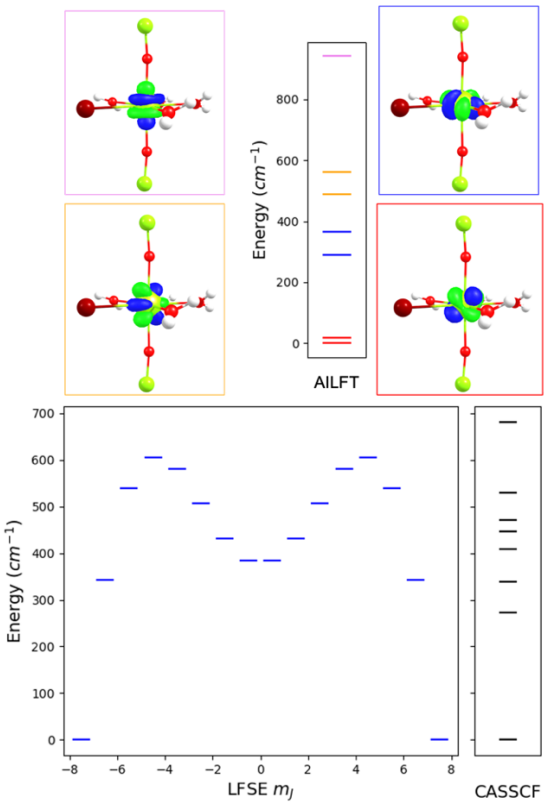

Figure 6. (top) f-orbital energy splitting obtained from AILFT calculations, blue, red, orange, and violet levels correspond to $f_{\pm3}$, $f_{\pm2}$, $f_{\pm1}$ and f_0 orbitals, respectively. One orbital for each block is depicted next to their corresponding levels, where atoms not belonging to the immediate coordination environment of the Dy^{III} ion are omitted for clarity. (bottom) LFSE and CASSCF energy levels (in cm^{-1}) for **1** are represented in blue and black colours, respectively.

The effect of the f-orbital splitting in the observed magnetic anisotropy can be investigated in further detail by considering the individual contributions of each $f_{\pm n}$ orbital block to the demagnetisation barrier, as shown previously by some of us.[89] In the case of **1**, the high axiality of the coordination environment dictates an orbital splitting where the most destabilized orbital corresponds to the f_0 (f_{z^3}) orbital, laying along the z-axis with an energy of 854 cm^{-1} (violet level in Figure 6, top). Interestingly, the most stable orbital block is not the one lying on the xy plane ($f_{y(3x^2-y^2)}$ and $f_{x(x^2-3y^2)}$ orbitals, collectively named $f_{\pm3}$) but the next block, which functions have a first order dependency with respect to z (f_{xyz} and $f_{z(x^2-y^2)}$ orbitals, collectively named $f_{\pm2}$) (red levels in Figure 6, top). Figure 6 (bottom) compares the CASSCF energies of the m_j sublevels of the ground $^6H_{15/2}$ multiplet with the ones derived from the orbital energies weighted by their

contributions to each sublevel in a ligand field stabilization energy (LFSE) approach.[89] The agreement between both data sets is satisfactory as both present an isolated ground doublet, separated by ca. 300 cm^{-1} from a dense pack of seven doublets spanning around 300-400 cm^{-1}. The pattern of the double well resembles a "M" letter, like the pattern derived from CASSCF (Figure 5, top). Considering that magnetic relaxation probably proceeds by the first excited doublet, the contribution of each orbital block to anisotropy can be estimated from the LFSE energy difference between the m_j = ±13/2 and m_j = ±15/2 states, which is $2/3 * (E_{f_{\pm 1}} - E_{f_{\pm 2}})$. In this case, the average energy of the $f_{\pm 1}$ and $f_{\pm 2}$ orbital blocks is 9.5 cm^{-1} and 523.7 cm^{-1}, resulting in a gap of 342.8 cm^{-1}.

Model assessment

The accuracy of the presented model can be evaluated for **1** since the temperature dependence of the relaxation time was successfully fitted to the combination of tunnelling, Raman and Orbach contributions. Employing Eq. 7, the ZFC curve can be simulated, and the maximum is obtained numerically. The effect of different demagnetisation mechanisms can be analysed by modifying the *τ(T)*curve to include diverse combinations of Orbach, tunnel, and Raman mechanisms. Our analysis starts with the ZFC/FC determined using a field of 500 Oe. At this field, the tunnelling mechanism should be mostly suppressed so only the Orbach and Raman mechanisms will be considered in the integration of $\tau^{-1}(T)$. It is important to stress that the heating step in ZFC/FC measurements is done with an external magnetic field which can affect demagnetisation parameters, especially tunnelling. Thus, care must be taken to account for this effect. Figure 7 presents the simulated ZFC curves for all the experimentally determined heating rates (0.01 K/min-5 K/min). Pleasingly, the position of the ZFC maxima is similar to the temperature range of the experiment (vide supra). In the same way as the analysis of the experimental ZFC/FC curves, data associated with the slower heating rates show ZFC curves where the $T_{B\text{-}ZFC/FC}$ is clearly discernible, while the faster heating rates show a less clear maximum.

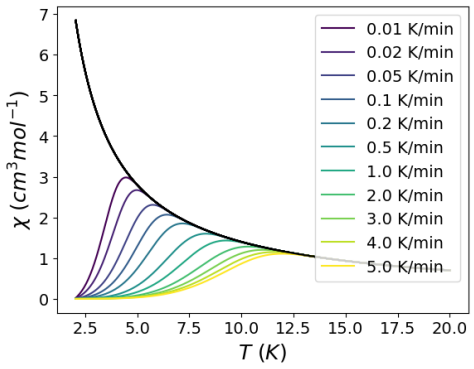

Figure 7. Simulated ZFC/FC curve for the sum of Orbach and Raman mechanisms, using the demagnetisation parameters fitted for **1**. C_1' was assumed to be one and the susceptibility was fixed to χT = 14.17 cm^3Kmol^{-1}.

The former simulations are now repeated incorporating tunnelling relaxation to the integration of $\tau^{-1}(T)$. The reference experimental data is now the ZFC/FC curve measured at 50 Oe, which should present a smaller quenching of tunnelling than the 500 Oe results. Figure 8 shows the simulated curves under these conditions. The comparison between Figures 7 and 8 clearly indicates that tunnelling is efficient in lowering the $T_{B\text{-}ZFC/FC}$ for **1**, in the same way that ZFC/FC data at 500 Oe show larger blocking temperatures than 50 Oe results. This highlights an important and probably overlooked experimental parameter that affects the blocking temperatures measured by ZFC/FC experiments: the external field necessary to record the magnetic moment along the temperature program, which adds to the importance of reporting the heating rate in these experiments.

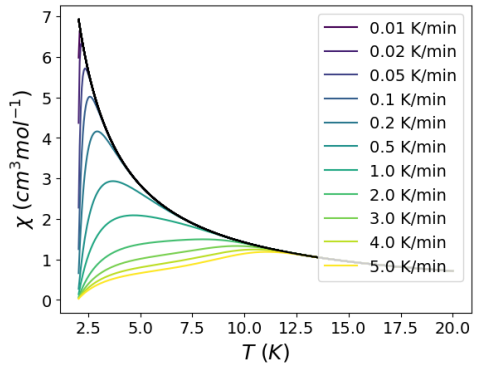

Figure 8. Simulated ZFC/FC curve for the sum of tunnelling, Orbach and Raman mechanisms, using the demagnetisation parameters fitted for **z**. C_1' was assumed to be one and the susceptibility was fixed to χT = 14.17 cm^3Kmol^{-1}.

A more quantitative comparison between the experimental and calculated blocking temperatures is presented in Figure 9. As mentioned earlier, the model can capture the effect of tunnelling in **1**, which diminishes the blocking temperature by around 5K. The agreement is quantitative at low heating rates but departs for faster programs (see red dashed line in Figure 9). Small modifications to the tunnelling value reveal a high sensitivity of the blocking temperature, where correcting the tunnelling time by a factor of 0.25 provides a simulated curve that agrees with the 50 Oe experiment in the complete range of heating rates (dot-dashed red line in Figure 9). This factor might seem a drastic correction, but it is significantly lower than the error bars of the magnetisation decay measurements calculated from the β parameter, according to Chilton and coworkers.[90] In this case, the range of relaxation times is even larger since a combination of magnetisation decay and ac-susceptibility are combined. The 500 Oe data also agrees with simulations, where the low heating rate results agree perfectly and depart by a couple of K at faster rates. Overall, the performance of the model is satisfactory since it allowed us to predict $T_{B\text{-}ZFC/FC}$ accurately and capture the heating rate dependency.

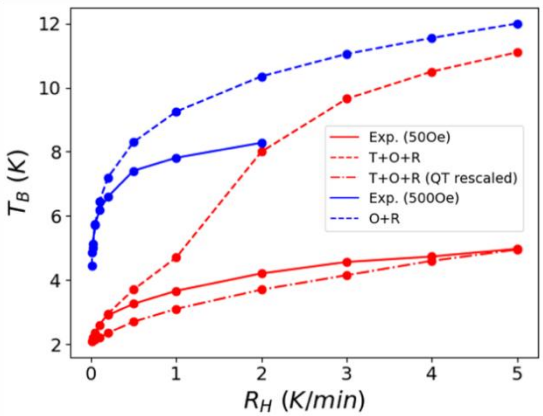

Figure 9. Comparison between experimental (solid lines) and simulated (dashed or dot-dashed lines) blocking temperatures. Data corresponding to 50 Oe and 500 Oe measurements are depicted in red and blue colours, respectively.

The demagnetisation mechanism limiting the blocking temperature can be estimated by repeating the same simulations including each demagnetisation mechanism separately. The tunnelling mechanism limits T_B to 2-3K for slow heating rates while it keeps most of the magnetic moment frozen at faster temperature programs, without reaching a maximum in the simulated temperature range (2-20K) (See Figure S12, left). The Raman-only simulation is similar to the one Orbach+Raman results from Figure 8, indicating that Raman relaxation is responsible for the simulated blocking between 4-12K. The Orbach-only plot shows blocking temperatures in a higher temperature range (14K-17K). Hence, it does not determine the value of T_B in this case (see Figure S12, right).

To assess the broader accuracy of the presented approach, a literature search for experimental examples of $T_{B\text{-}ZFC/FC}$ was performed. Such values can be also obtained for any single-molecule magnet system by introducing the spin relaxation parameters on the web page https://tbzfcfc.streamlit.app. By reconstructing the $\tau(T)$ curve using fitted parameters, we can calculate T_B using Eq. 7. Unfortunately, the heating rate is not always informed, so we have assumed lower and higher limit values for this parameter when R_H information is missing (0.2 K/min and 5 K/min to account for a slow and fast sweeping rate).

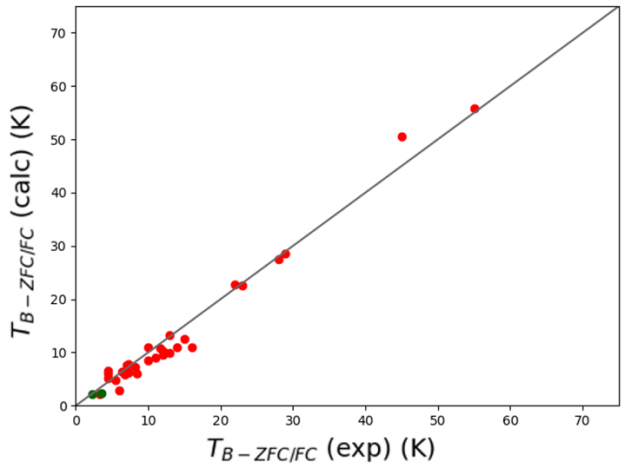

Figure 10. Comparison between the experimental zero-field cooling/field cooling blocking temperatures and the ones calculated using Eq. 12. Only 37 cases (35 lanthanide and two transition metal compounds depicted in red and green, respectively) with a reported heating rate are considered (see Fig. 11 for the other systems). The black line represents the perfect agreement between both values.

Table S9 compares experimental and predicted values for ZFC/FC blocking temperatures for 97 lanthanide SMMs reported in literature.[13, 14, 37, 38, 41, 50, 51, 60, 61, 63, 65, 91-136] and nine transition metal complexes[137-145] The lanthanide benchmark set contains mononuclear and polynuclear complexes based on Dy^{III}, Tb^{III}, Er^{III} and Ho^{III} ions, heteronuclear complexes containing Dy^{III} or Tb^{III} ions and transition metals, and diluted systems. The nine transition compounds are Mn_{12} complexes, tetranuclear and mononuclear iron and cobalt complexes. The fitting parameters for ac-susceptibility data range from systems involving combinations of Orbach, Raman, and tunnelling, Orbach and Raman, Orbach and tunnelling, Raman and tunnelling, to Orbach-only terms. Besides, the list includes complexes exhibiting two or three relaxation processes, where one of them (usually the main process) was considered to calculate T_B. As is observed in this list, some authors inform the T_{irrev} (indicated with an asterisk) instead $T_{B\text{-}ZFC/FC}$, and others report both values. It is possible to observe that T_{irrev} is always higher than $T_{B\text{-}ZFC/FC}$ value, as expected. In some cases, the difference between T_{irrev} and $T_{B\text{-}ZFC/FC}$ values exceeds 10 K (e.g 78 K and ~55 K, respectively, for complex 3 in Table S9). Another issue to highlight is the lack of information about the heating rate (R_H). For 97 lanthanide complexes in Table S9, R_H value was only included in the original paper for 35 complexes, while only for two transition metal complexes (see Figure 10). Reported R_H values ranging from 0.189 to 5 K/min, demonstrating that there is no consensus on this important parameter that defines the T_B value. In most cases, the reported $T_{B\text{-}ZFC/FC}$ lies in the range of T_B obtained with R_H of 0.2 K/min and 5 K/min, or close to these values (see Figure 11). Similarly, when R_H is informed, the obtained T_B with this heating rate is close to the reported $T_{B\text{-}ZFC/FC}$ (see Figure 10), demonstrating the accuracy and broad applicability of the presented approach.

The large amount of data collected in Table S9 allows to investigate if a fixed relaxation time like $T_{B\text{-}100}$ can be useful as a descriptor for ZFC/FC blocking temperatures. Figure S15 presents the relaxation time at the experimental $T_{B\text{-}ZFC/FC}$ for the data presented in Table S9 as a function of the heating rate. Clusters of data are observed around the most common R_H values (0.2-04 K/min, 2 K/min and 5 K/min). In all cases, a high dispersion of relaxation times is observed, especially for slow heating rates. In the case of the cluster ranging 0.2-04 K/min, the maximum and minimum relaxation times are 282 s and 1 s. Thus, a unique reference relaxation time cannot be used to define ZFC/FC blocking temperatures, even at a fixed heating rate.

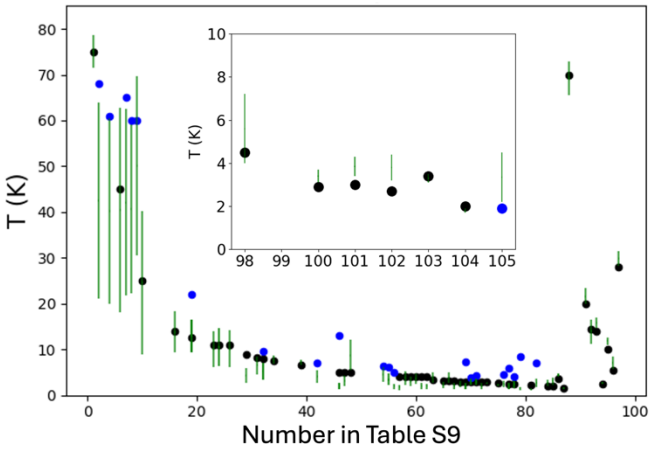

Figure 11. Comparison between the experimental $T_{B\text{-}ZFC}$ blocking (black dots) or T_{irrev} irreversible (blue dots, values in Table S9 indicated with an asterisk) temperatures for the 62 lanthanide systems (7 transition metal systems in the inset) without reported heating rate. The x-axis indicates the complex number in Table S9. The green bar corresponds to the limit values calculated using Eq. 12 using with R_H 0.2 K/min and 5 K/min.

For systems without the reported heating rate value, the limiting values of the blocking temperature calculated with R_H 0.2 K/min and 5 K/min are shown in Fig. 11. As can be seen, in practically all

cases, the $T_{B\text{-}ZFC/FC}$ value falls within the calculated range. However, the T_{irrev} values are outside of the bar limits but always above in agreement with the fact that the irreversibility temperature (T_{irrev}) must be higher than $T_{B\text{-}ZFC}$.[78]

Conclusions

This work discusses the various metrics for quantifying blocking temperatures and the challenges associated with each method. The new proposed approach for estimating $T_{B\text{-}ZFC/FC}$ from ac-susceptibility parameters offers a practical way to compare the performance of SMMs in the literature and estimate $T_{B\text{-}ZFC}$ without the need for extensive measurements. Thus, the $T_{B\text{-}ZFC}$ blocking temperature for a given heating rate can be estimated from the relaxation time data, which is the most common magnetic characterization in SMMs. In this context, the synthesis and characterization of the Dy^{III} SMM with D_{5h} symmetry, $[Dy(OPAd_2Bz)_2(H_2O)_4Br]Br_2{\cdot}4THF$ (**1**) allowed to test the predictions for the blocking temperature in a broad range of heating rates and two different static magnetic fields. Furthermore, complex **1** is an interesting example of an air and humidity-stable SMM with high U_{eff} and T_B values, adding to the scarce list of examples of SMMs with D_{5h} symmetry.

Magnetic measurements confirm the SMM behaviour of complex **1**, with a ZFC/FC blocking temperature in the range of 2.5K-8K, depending on the heating rate and the magnitude of the probe magnetic field. The presence of magnetic hysteresis and the large coercive field and remanent magnetisation values further support its SMM properties. Additionally, AC magnetic susceptibility measurements reveal a high magnetisation reversal barrier, indicating slow relaxation of magnetisation. Ab initio calculations provide insight into the electronic structure and relaxation mechanism of complex **1**. The calculations confirm the strong uniaxial magnetic anisotropy and reveal that magnetic relaxation occurs primarily via the first excited state (KD2).

In summary, the study of complex **1** exemplifies the potential of stable SMMs with D_{5h} geometry and axial ligands in achieving high-performance SMMs. The proposed approach for estimating $T_{B\text{-}ZFC}$ provided accurate values of the ZFC/FC blocking temperature of **1**, properly captured the heating rate and probe field dependence of $T_{B\text{-}ZFC/FC,}$ and identified the Raman and tunnelling mechanisms as the ones determining the blocking temperature. The possibility of relating the spin relaxation mechanisms directly to the blocking temperature opens a way for a better understanding on T_B tuning, which is a fundamental parameter of SMMs. Furthermore, the proposal successfully predicted blocking temperatures for many literature examples of SMMs, offering a valuable tool for characterizing and comparing SMMs in future research.

Author contributions

Y. G. and M. A. P.: investigation, data analysis D. A.: software; M. M. Q. M., E. C., S. G. C., E. R. and D. A.: conceptualization, investigation, data analysis, validation, supervision, resources, funding acquisition; all authors contributed to the writing and editing of the article.

Conflicts of interest

There are no conflicts to declare.

Data availability

The data supporting this article have been included as part of the ESI. Estimation of the blocking temperature for any single-molecule magnet system by introducing the spin relaxation parameters on the web page https://tbzfcfc.streamlit.app.

Acknowledgements

D.A. thanks FONDECYT Regular 1210325 for financial support. Powered@NLHPC: this research was partially supported by the supercomputing infrastructure of the NLHPC (ECM-02). Financial support from Ministerio de Ciencia e Innovación (projects PID2022-138090NB-C21, PID2021-122464NB-I00, TED2021-129593B-I00 and Maria de Maeztu CEX2021-001202-M), Junta de Andalucía (FQM-195 and and FQM-337), FEDER/Junta de Andalucía (projects I + D + i P20_00692, C-EXP-140-UGR23 and M.1.B.B TA_000722, Programas Operativos FEDER 2014-2020 y 2021-2027, Consejería de Economía, Conocimiento, Empresas y Universidad), and the University of Granada (project I + D + i PPJIA2020.10) is greatly acknowledged. The authors also acknowledge the Centro de Servicios de Informática y Redes de Comunicaciones (CSIRC) for computational time and facilities. M. M. Q. M. thanks Ministerio de Ciencia e Innovación for a Ramón y Cajal contract (the publication is part of the project PID2022-138090NB-C21 and the grant RYC2021-034288-I funded by MCIN/AEI/10.13039/501100011033 and by the European Union «NextGenerationEU»/PRTR»). E.R. also acknowledges the Generalitat de Catalunya for an ICREA Academia and 2021-SGR-00286 grants, and for computational resources to CSUC.

We want to dedicate this paper to Prof. Miquel Julve from the Universitat de Valencia, who recently passed away.

Notes and references

1 S. M. J. Aubin, M. W. Wemple, D. M. Adams, H.-L. Tsai, G. Christou and D. N. Hendrickson, Distorted $Mn^{IV}Mn^{III}_3$ Cubane Complexes as Single-Molecule Magnets. *J. Am. Chem. Soc.* 1996*,* ***118***, 7746-7754.

2 R. Sessoli, D. Gatteschi, A. Caneschi and M. A. Novak, Magnetic bistability in a metal-ion cluster. *Nature* 1993*,* ***365***, 141-143.

3 D. N. Woodruff, R. E. P. Winpenny and R. A. Layfield, Lanthanide Single-Molecule Magnets. *Chem. Rev., 20*13*,* ***113***, 5110-5148.

4 A. Zabala-Lekuona, J. M. Seco and E. Colacio, Single-Molecule Magnets: From Mn_{12}-ac to dysprosium metallocenes, a travel in time. *Coord. Chem. Rev., 20*21*,* ***441***, 213984.

5 N. F. Chilton, Molecular Magnetism. *Annu. Rev. Mater. Res., 20*22*,* ***52***, 79-101.

6 E. Coronado, Molecular magnetism: from chemical design to spin control in molecules, materials and devices. *Nat. Rev. Mater., 20*19*,* ***5***, 87-104.

7 A. Gaita-Ariño, F. Luis, S. Hill and E. Coronado, Molecular spins for quantum computation. *Nat Chem,* 2019*,* ***11***, 301-309.

8 J. Long, Y. Guari, R. A. S. Ferreira, L. D. Carlos and J. Larionova, Recent advances in luminescent lanthanide based Single-Molecule Magnets. *Coord. Chem. Rev., 20*18*,* ***363***, 57-70.

9 R. Marin, G. Brunet and M. Murugesu, Shining New Light on Multifunctional Lanthanide Single-Molecule Magnets. *Angew. Chem. Int. Ed., 2020, **60**,* 1728-1746.

10 E. Moreno-Pineda and W. Wernsdorfer, Measuring molecular magnets for quantum technologies. *Nat. Rev. Phys., 2021, **3**,* 645-659.

11 M. Shiddiq, D. Komijani, Y. Duan, A. Gaita-Ariño, E. Coronado and S. Hill, Enhancing coherence in molecular spin qubits via atomic clock transitions. *Nature,* 2016, ***531***, 348-351.

12 R. Vincent, S. Klyatskaya, M. Ruben, W. Wernsdorfer and F. Balestro, Electronic read-out of a single nuclear spin using a molecular spin transistor. *Nature,* 2012, ***488***, 357-360.

13 F. Liu, D. S. Krylov, L. Spree, S. M. Avdoshenko, N. A. Samoylova, M. Rosenkranz, A. Kostanyan, T. Greber, A. U. B. Wolter, B. Büchner and A. A. Popov, Single molecule magnet with an unpaired electron trapped between two lanthanide ions inside a fullerene. *Nat. Commun., 2017, **8***, 16098.

14 F. Liu, G. Velkos, D. S. Krylov, L. Spree, M. Zalibera, R. Ray, N. A. Samoylova, C.-H. Chen, M. Rosenkranz, S. Schiemenz, F. Ziegs, K. Nenkov, A. Kostanyan, T. Greber, A. U. B. Wolter, M. Richter, B. Büchner, S. M. Avdoshenko and A. A. Popov, Air-stable redox-active nanomagnets with lanthanide spins radical-bridged by a metal–metal bond. *Nat. Commun., 2019, **10***, 571.

15 B. M. Day, F.-S. Guo and R. A. Layfield, Cyclopentadienyl Ligands in Lanthanide Single-Molecule Magnets: One Ring To Rule Them All? *Acc. Chem. Res., 2018, **51***, 1880-1889.

16 A. Dey, P. Kalita and V. Chandrasekhar, Lanthanide(III)-Based Single-Ion Magnets. *ACS Omega,* 2018, ***3***, 9462-9475.

17 K. L. M. Harriman and M. Murugesu, An Organolanthanide Building Block Approach to Single-Molecule Magnets. *Acc. Chem. Res., 2016, **49***, 1158-1167.

18 J.-L. Liu, Y.-C. Chen and M.-L. Tong, Symmetry strategies for high performance lanthanide-based single-molecule magnets. *Chem. Soc. Rev., 2018, **47***, 2431-2453.

19 J. Tang and P. Zhang, Dinuclear Lanthanide Single-Molecule Magnets. In *Lanthanide Single Molecule Magnets*, Springer Berlin Heidelberg: 2015; pp 91-126.

20 J. Wang, C. Y. Sun, Q. Zheng, D. Q. Wang, Y. T. Chen, J. F. Ju, T. M. Sun, Y. Cui, Y. Ding and Y. F. Tang, Lanthanide Single-molecule Magnets: Synthetic Strategy, Structures, Properties and Recent Advances. *Chem. Asian J., 2023, **18***, e202201297.

21. A. J. Brown, D. Pinkowicz, M. R. Saber and K. R. Dunbar, A Trigonal-Pyramidal Erbium(III) Single-Molecule Magnet, *Angew. Chem. Int. Ed.*, 2015, **54**, 5864-5868.

22. Y. Chen, F. Ma, X. Chen, B. Dong, K. Wang, S. Jiang, C. Wang, X. Chen, D. Qi, H. Sun, B. Wang, S. Gao and J. Jiang, A New Bis(phthalocyaninato) Terbium Single-Ion Magnet with an Overall Excellent Magnetic Performance, *Inorg. Chem.*, 2017, **56**, 13889-13896.

23. C. R. Ganivet, B. Ballesteros, G. de la Torre, J. M. Clemente-Juan, E. Coronado and T. Torres, Influence of Peripheral Substitution on the Magnetic Behavior of Single-Ion Magnets Based on Homo- and Heteroleptic Tb^{III} Bis(phthalocyaninate), *Chem. Eur. J.*, 2013, **19**, 1457-1465.

24. N. Ishikawa, M. Sugita, N. Tanaka, T. Ishikawa, S.-y. Koshihara and Y. Kaizu, Upward Temperature Shift of the Intrinsic Phase Lag of the Magnetization of Bis(phthalocyaninato)terbium by Ligand Oxidation Creating an S = 1/2 Spin, *Inorg. Chem.*, 2004, **43**, 5498-5500.

25. W.-J. Xu, Q.-C. Luo, Z.-H. Li, Y.-Q. Zhai and Y.-Z. Zheng, Bis-Alkoxide Dysprosium(III) Crown Ether Complexes Exhibit Tunable Air Stability and Record Energy Barrier, *Adv. Sci.*, 2024, **11**, 2308548.

26. Z.-H. Li, Y.-Q. Zhai, W.-P. Chen, Y.-S. Ding and Y.-Z. Zheng, *ChemRxiv*, 2019, DOI: 10.26434/chemrxiv.9606206.v1.

27. F. Benner, L. La Droitte, O. Cador, B. Le Guennic and S. Demir, Magnetic hysteresis and large coercivity in bisbenzimidazole radical-bridged dilanthanide complexes, *Chem. Sci.*, 2023, **14**, 5577-5592.

28. J. Tang, I. Hewitt, N. T. Madhu, G. Chastanet, W. Wernsdorfer, C. E. Anson, C. Benelli, R. Sessoli and A. K. Powell, Dysprosium Triangles Showing Single-Molecule Magnet Behavior of Thermally Excited Spin States, *Angew. Chem. Int. Ed.*, 2006, **45**, 1729-1733.

29. P. Zhang, F. Benner, N. F. Chilton and S. Demir, Organometallic lanthanide bismuth cluster single-molecule magnets, *Chem*, 2022, **8**, 717-730.

30. N. F. Chilton, C. A. P. Goodwin, D. P. Mills and R. E. P. Winpenny, The first near-linear bis(amide) f-block complex: a blueprint for a high temperature single molecule magnet, *Chem. Commun.*, 2015, **51**, 101-103.

31. J. D. Rinehart and J. R. Long, Exploiting single-ion anisotropy in the design of f-element single-molecule magnets, *Chem. Sci.*, 2011, **2**, 2078.

32. L. Ungur and L. F. Chibotaru, Strategies toward High-Temperature Lanthanide-Based Single-Molecule Magnets, *Inorg. Chem.*, 2016, **55**, 10043-10056.

33. S. Dey, T. Sharma and G. Rajaraman, Unravelling the role of spin–vibrational coupling in designing high-performance pentagonal bipyramidal Dy(iii) single ion magnets, *Chem. Sci.*, 2024, **15**, 6465-6477.

34. S. Mondal and A. Lunghi, Unraveling the Contributions to Spin–Lattice Relaxation in Kramers Single-Molecule Magnets, *J. Am. Chem. Soc.*, 2022, **144**, 22965-22975.

35. V. Vieru, S. Gómez-Coca, E. Ruiz and L. F. Chibotaru, Increasing the Magnetic Blocking Temperature of Single-Molecule Magnets, *Angew. Chem. Int. Ed.*, 2024, **63**, e202303146.

36. T. Sharma, A. Swain and G. Rajaraman, *ChemRxiv*, 2023, DOI: doi:10.26434/chemrxiv-2023-wpc4r.

37. F.-S. Guo, B. M. Day, Y.-C. Chen, M.-L. Tong, A. Mansikkamäki and R. A. Layfield, Magnetic hysteresis up to 80 kelvin in a dysprosium metallocene single-molecule magnet, *Science*, 2018, **362**, 1400-1403.

38. C. A. Gould, K. R. McClain, D. Reta, J. G. C. Kragskow, D. A. Marchiori, E. Lachman, E.-S. Choi, J. G. Analytis, R. D. Britt, N. F. Chilton, B. G. Harvey and J. R. Long, Ultrahard magnetism from mixed-valence dilanthanide complexes with metal-metal bonding, *Science*, 2022, **375**, 198-202.

39. D. Aravena and E. Ruiz, Shedding Light on the Single-Molecule Magnet Behavior of Mononuclear Dy^{III} Complexes, *Inorg. Chem.*, 2013, **52**, 13770-13778.

40. N. F. Chilton, D. Collison, E. J. L. McInnes, R. E. P. Winpenny and A. Soncini, An electrostatic model for the determination of magnetic anisotropy in dysprosium complexes, *Nat. Commun.*, 2013, **4**, 3551.

41. M. Gregson, N. F. Chilton, A.-M. Ariciu, F. Tuna, I. F. Crowe, W. Lewis, A. J. Blake, D. Collison, E. J. L. McInnes, R. E. P. Winpenny and S. T. Liddle, A monometallic lanthanide bis(methanediide) single molecule magnet with a large energy barrier and complex spin relaxation behaviour, *Chem. Sci.*, 2016, **7**, 155-165.

42. S. T. Liddle and J. van Slageren, Improving f-element single molecule magnets, *Chem. Soc. Rev.*, 2015, **44**, 6655-6669.

43. K. L. M. Harriman, J. L. Brosmer, L. Ungur, P. L. Diaconescu and M. Murugesu, Pursuit of Record Breaking Energy Barriers: A

Study of Magnetic Axiality in Diamide Ligated Dy^{III} Single-Molecule Magnets, *J. Am. Chem. Soc.*, 2017, **139**, 1420-1423.

44. P. Zhang, L. Zhang, C. Wang, S. Xue, S.-Y. Lin and J. Tang, Equatorially Coordinated Lanthanide Single Ion Magnets, *J. Am. Chem. Soc.*, 2014, **136**, 4484-4487.
45. M. A. AlDamen, J. M. Clemente-Juan, E. Coronado, C. Martí-Gastaldo and A. Gaita-Ariño, Mononuclear Lanthanide Single-Molecule Magnets Based on Polyoxometalates, *J. Am. Chem. Soc.*, 2008, **130**, 8874-8875.
46. P.-E. Car, M. Perfetti, M. Mannini, A. Favre, A. Caneschi and R. Sessoli, Giant field dependence of the low temperature relaxation of the magnetization in a dysprosium(iii)–DOTA complex, *Chem. Commun.*, 2011, **47**, 3751.
47. K. Katoh, S. Yamashita, N. Yasuda, Y. Kitagawa, B. K. Breedlove, Y. Nakazawa and M. Yamashita, Frontispiece: Control of the Spin Dynamics of Single-Molecule Magnets by using a Quasi One-Dimensional Arrangement, *Angew. Chem. Int. Ed.*, 2018, **57**, 9262-9267.
48. L. Sorace, C. Benelli and D. Gatteschi, Lanthanides in molecular magnetism: old tools in a new field, *Chem. Soc. Rev.*, 2011, **40**, 3092-3104.
49. A.M.Atkin, M.J.Giansiracusa, S.Calvello, E.Rousset, R.W.Gable, W.Phonsri, K.S.Murray, J.K.Howard, A.Soncini, R.A.Mole and C.Boskovic, bis(2,2'-bipyridine)-(methanol)-[3,4,5,6-tetrabromobenzene-1,2-diolato]-(3,4,5,6 tetrabromobenzene-1,2-diolato)-dysprosium(iii), *Inorg.Chem.*, 2023, **62**, 1141.
50. C. A. P. Goodwin, F. Ortu, D. Reta, N. F. Chilton and D. P. Mills, Molecular magnetic hysteresis at 60 kelvin in dysprosocenium, *Nature*, 2017, **548**, 439-442.
51. F.-S. Guo, B. M. Day, Y.-C. Chen, M.-L. Tong, A. Mansikkamäki and R. A. Layfield, A Dysprosium Metallocene Single-Molecule Magnet Functioning at the Axial Limit, *Angew. Chem. Int. Ed.*, 2017, **56**, 11445-11449.
52. S.-D. Jiang, B.-W. Wang, H.-L. Sun, Z.-M. Wang and S. Gao, An Organometallic Single-Ion Magnet, *J. Am. Chem. Soc.*, 2011, **133**, 4730-4733.
53. L. Münzfeld, C. Schoo, S. Bestgen, E. Moreno-Pineda, R. Köppe, M. Ruben and P. W. Roesky, Synthesis, structures and magnetic properties of $[(\eta_9\text{-}C_9H_9)Ln(\eta_8\text{-}C_8H_8)]$ super sandwich complexes, *Nat. Commun.*, 2019, **10**.
54. A. H. Vincent, Y. L. Whyatt, N. F. Chilton and J. R. Long, Strong Axiality in a Dysprosium(III) Bis(borolide) Complex Leads to Magnetic Blocking at 65 K, *J. Am. Chem. Soc.*, 2023, **145**, 1572-1579.
55. A. B. Canaj, S. Dey, C. Wilson, O. Céspedes, G. Rajaraman and M. Murrie, Engineering macrocyclic high performance pentagonal bipyramidal Dy(iii) single-ion magnets, *Chem. Commun.*, 2020, **56**, 12037-12040.
56. A. B. Canaj, M. K. Singh, C. Wilson, G. Rajaraman and M. Murrie, Chemical and *in silico* tuning of the magnetisation reversal barrier in pentagonal bipyramidal Dy(iii) single-ion magnets, *Chem. Commun.*, 2018, **54**, 8273-8276.
57. Y.-C. Chen, J.-L. Liu, Y. Lan, Z.-Q. Zhong, A. Mansikkamäki, L. Ungur, Q.-W. Li, J.-H. Jia, L. F. Chibotaru, J.-B. Han, W. Wernsdorfer, X.-M. Chen and M.-L. Tong, Dynamic Magnetic and Optical Insight into a High-Performance Pentagonal Bipyramidal Dy^{III} Single-Ion Magnet, *Chem. Eur. J.*, 2017, **23**, 5630-5630.
58. Y.-C. Chen, J.-L. Liu, L. Ungur, J. Liu, Q.-W. Li, L.-F. Wang, Z.-P. Ni, L. F. Chibotaru, X.-M. Chen and M.-L. Tong, Symmetry-Supported Magnetic Blocking at 20 K in Pentagonal Bipyramidal Dy(III) Single-Ion Magnets, *J. Am. Chem. Soc.*, 2016, **138**, 2829-2837.
59. I. F. Díaz-Ortega, J. M. Herrera, S. Dey, H. Nojiri, G. Rajaraman and E. Colacio, The effect of the electronic structure and flexibility of the counteranions on magnetization relaxation in $[Dy(L)_2(H_2O)_5]^{3+}$ (L = phosphine oxide derivative) pentagonal bipyramidal SIMs, *Inorg. Chem. Front.*, 2020, **7**, 689-699.
60. Y.-S. Ding, N. F. Chilton, R. E. P. Winpenny and Y.-Z. Zheng, On Approaching the Limit of Molecular Magnetic Anisotropy: A Near-Perfect Pentagonal Bipyramidal Dysprosium(III) Single-Molecule Magnet, *Angew. Chem. Int. Ed.*, 2016, **55**, 16071-16074.
61. Y. S. Ding, T. Han, Y. Q. Zhai, D. Reta, N. F. Chilton, R. E. P. Winpenny and Y. Z. Zheng, A Study of Magnetic Relaxation in Dysprosium(III) Single-Molecule Magnets, *Chem. Eur. J.*, 2020, **26**, 5893-5902.
62. S. K. Gupta, T. Rajeshkumar, G. Rajaraman and R. Murugavel, An air-stable Dy(iii) single-ion magnet with high anisotropy barrier and blocking temperature, *Chem. Sci.*, 2016, **7**, 5181-5191.
63. Z. Jiang, L. Sun, Q. Yang, B. Yin, H. Ke, J. Han, Q. Wei, G. Xie and S. Chen, Excess axial electrostatic repulsion as a criterion for pentagonal bipyramidal Dy^{III} single-ion magnets with high U_{eff} and TB, *J. Mater. Chem. C*, 2018, **6**, 4273-4280.
64. L.-L. Li, H.-D. Su, S. Liu, Y.-C. Xu and W.-Z. Wang, A new air- and moisture-stable pentagonal-bipyramidal Dy^{III} single-ion magnet based on the HMPA ligand, *Dalton Trans.*, 2019, **48**, 2213-2219.
65. J. Liu, Y.-C. Chen, J.-L. Liu, V. Vieru, L. Ungur, J.-H. Jia, L. F. Chibotaru, Y. Lan, W. Wernsdorfer, S. Gao, X.-M. Chen and M.-L. Tong, A Stable Pentagonal Bipyramidal Dy(III) Single-Ion Magnet with a Record Magnetization Reversal Barrier over 1000 K, *J. Am. Chem. Soc.*, 2016, **138**, 5441-5450.
66. J.-L. Liu, Y.-C. Chen, Y.-Z. Zheng, W.-Q. Lin, L. Ungur, W. Wernsdorfer, L. F. Chibotaru and M.-L. Tong, Switching the anisotropy barrier of a single-ion magnet by symmetry change from quasi-D_{5h} to quasi-O_h, *Chem. Sci.*, 2013, **4**, 3310.
67. J. Long, A. N. Selikhov, E. Mamontova, K. A. Lyssenko, Y. Guari, J. Larionova and A. A. Trifonov, Single-molecule magnet behaviour in a Dy(iii) pentagonal bipyramidal complex with a quasi-linear Cl–Dy–Cl sequence, *Dalton Trans.*, 2019, **48**, 35-39.
68. H. Wu, M. Li, B. Yin, Z. Xia, H. Ke, Q. Wei, G. Xie, S. Chen and S. Gao, Fine-tuning the type of equatorial donor atom in pentagonal bipyramidal Dy(iii) complexes to enhance single-molecule magnet properties, *Dalton Trans.*, 2019, **48**, 16384-16394.
69. B. Zhang, X. Guo, P. Tan, W. Lv, X. Bai, Y. Zhou, A. Yuan, L. Chen, D. Liu, H.-H. Cui, R. Wang and X.-T. Chen, Axial Ligand as a Critical Factor for High-Performance Pentagonal Bipyramidal Dy(III) Single-Ion Magnets, *Inorg. Chem.*, 2022, **61**, 19726-19734.
70. L. Zhu, Y. Dong, B. Yin, P. Ma and D. Li, Improving the single-molecule magnet properties of two pentagonal bipyramidal Dy^{3+} compounds by the introduction of both electron-withdrawing and -donating groups, *Dalton Trans.*, 2021, **50**, 12607-12618.
71. Y. Ma, Y.-Q. Zhai, Q.-C. Luo, Y.-S. Ding and Y.-Z. Zheng, Ligand Fluorination to Mitigate the Raman Relaxation of Dy^{III} Single-Molecule Magnets: A Combined Terahertz, Far-IR and Vibronic Barrier Model Study, *Angew. Chem. Int. Ed.*, 2022, **61**, e202206022.

72. X. Ding, Q. Luo, Y. Zhai, X. Zhang, Y. Lv, X. Zhang, C. Ke, C. Wu and Y. Zheng, Rigid Dysprosium(III) Single-Molecule Magnets Exhibit Preserved Superparamagnetism in Solution, *Chin. J. Chem .* 2022, **40**, 563-570.
73. K.-X. Yu, Y.-S. Ding, Y.-Q. Zhai, T. Han and Y.-Z. Zheng, Equatorial coordination optimization for enhanced axiality of mononuclear Dy(iii) single-molecule magnets, *Dalton Trans.*, 2020, **49**, 3222-3227.
74. I. Oyarzabal, J. Ruiz, E. Ruiz, D. Aravena, J. M. Seco and E. Colacio, Increasing the effective energy barrier promoted by the change of a counteranion in a Zn–Dy–Zn SMM: slow relaxation via the second excited state, *Chem. Commun.*, 2015, **51**, 12353-12356.
75. S. K. Singh, T. Gupta, M. Shanmugam and G. Rajaraman, Unprecedented magnetic relaxation via the fourth excited state in low-coordinate lanthanide single-ion magnets: a theoretical perspective, *Chem. Commun.*, 2014, **50**, 15513-15516.
76. M. Briganti, F. Santanni, L. Tesi, F. Totti, R. Sessoli and A. Lunghi, A Complete *Ab Initio* View of Orbach and Raman Spin–Lattice Relaxation in a Dysprosium Coordination Compound, *J. Am. Chem. Soc.*, 2021, **143**, 13633-13645.
77. Y.-S. Ding, K.-X. Yu, D. Reta, F. Ortu, R. E. P. Winpenny, Y.-Z. Zheng and N. F. Chilton, Field- and temperature-dependent quantum tunnelling of the magnetisation in a large barrier single-molecule magnet, *Nat. Commun.*, 2018, **9**, 3134.
78. D. Gatteschi, R. Sessoli and J. Villain, Molecular Nanomagnets, 2006, 58-61, Oxford, Oxford Academic.
79. S. Alvarez, D. Avnir, M. Llunell and M. Pinsky, Continuous symmetry maps and shape classification. The case of six-coordinated metal compoundsElectronic supplementary information (ESI) available: tables of CSD refcodes, structural parameters and symmetry measures for the studied compounds. *New J. Chem.*, 2002, **26**, 996-1009.
80. D. Gatteschi, R. Sessoli and J. Villain, Molecular Nanomagnets, 2006, 108-159, Oxford, Oxford Academic.
81. R. Orbach, On the Theory of Spin-Lattice Relaxation in Paramagnetic Salts, *Proc. Phys. Soc.*, 1961, **77**, 821-826.
82. F. Neese, Software update: the ORCA program system, version 4.0, *Wiley Interdiscip. Rev. Comput. Mol. Sci.*, 2018, **8**, e1327.
83. F. Neese, Software update: The ORCA program system—Version 5.0, *Wiley Interdiscip. Rev. Comput. Mol. Sci., 2022, **12***, 1606.
84. F. Neese, F. Wennmohs, U. Becker and C. Riplinger, The ORCA quantum chemistry program package, *J. Chem. Phys.*, 2020, **152**, 224108.
85. F. Aquilante, J. Autschbach, R. K. Carlson, L. F. Chibotaru, M. G. Delcey, L. De Vico, I. Fdez. Galván, N. Ferré, L. M. Frutos, L. Gagliardi, M. Garavelli, A. Giussani, C. E. Hoyer, G. Li Manni, H. Lischka, D. Ma, P. Å. Malmqvist, T. Müller, A. Nenov, M. Olivucci, T. B. Pedersen, D. Peng, F. Plasser, B. Pritchard, M. Reiher, I. Rivalta, I. Schapiro, J. Segarra-Martí, M. Stenrup, D. G. Truhlar, L. Ungur, A. Valentini, S. Vancoillie, V. Veryazov, V. P. Vysotskiy, O. Weingart, F. Zapata and R. Lindh, Molcas 8: New capabilities for multiconfigurational quantum chemical calculations across the periodic table, *J. Comput. Chem.*, 2015, **37**, 506-541.
86. L. F. Chibotaru and L. Ungur, Ab initio calculation of anisotropic magnetic properties of complexes. I. Unique definition of pseudospin Hamiltonians and their derivation, *J. Chem. Phys.*, 2012, **137**, 064112.
87. A. A. Granovsky, Extended multi-configuration quasi-degenerate perturbation theory: The new approach to multi-state multi-reference perturbation theory, *J. Chem. Phys.*, 2011, **134**, 214113.
88. D. Aravena, Ab Initio Prediction of Tunneling Relaxation Times and Effective Demagnetization Barriers in Kramers Lanthanide Single-Molecule Magnets, *J. Phys. Chem. Lett., 2018, **9***, 5327-5333.
89. Y. Gil and D. Aravena, Understanding Single-Molecule Magnet properties of lanthanide complexes from 4f orbital splitting, *Dalton Trans.*, 2024, **53**, 2207-2217.
90. W. J. A. Blackmore, G. K. Gransbury, P. Evans, J. G. C. Kragskow, D. P. Mills and N. F. Chilton, Characterisation of magnetic relaxation on extremely long timescales, *PhysChemChemPhys*, 2023, **25**, 16735-16744.
91. J. C. Vanjak, B. O. Wilkins, V. Vieru, N. S. Bhuvanesh, J. H. Reibenspies, C. D. Martin, L. F. Chibotaru and M. Nippe, A High-Performance Single-Molecule Magnet Utilizing Dianionic Aminoborolide Ligands, *J. Am. Chem. Soc.*, 2022, **144**, 17743-17747.
92. K. Randall McClain, C. A. Gould, K. Chakarawet, S. J. Teat, T. J. Groshens, J. R. Long and B. G. Harvey, High-temperature magnetic blocking and magneto-structural correlations in a series of dysprosium(iii) metallocenium single-molecule magnets, *Chem. Sci.*, 2018, **9**, 8492-8503.
93. P. Evans, D. Reta, G. F. S. Whitehead, N. F. Chilton and D. P. Mills, Bis-Monophospholyl Dysprosium Cation Showing Magnetic Hysteresis at 48 K, *J. Am. Chem. Soc.*, 2019, **141**, 19935-19940.
94. K.-X. Yu, J. G. C. Kragskow, Y.-S. Ding, Y.-Q. Zhai, D. Reta, N. Chilton and Y.-Z. Zheng, Enhancing Magnetic Hysteresis in Single-Molecule Magnets by Ligand Functionalisation, *Chem* 2020, ***6***, 1777–1793.
95. L. R. Thomas-Hargreaves, M. J. Giansiracusa, M. Gregson, E. Zanda, F. O'Donnell, A. J. Wooles, N. F. Chilton and S. T. Liddle, Correlating axial and equatorial ligand field effects to the single-molecule magnet performances of a family of dysprosium bis-methanediide complexes, *Chem. Sci.*, 2021, **12**, 3911-3920.
96. P. Evans, D. Reta, C. A. P. Goodwin, F. Ortu, N. F. Chilton and D. P. Mills, A double-dysprosocenium single-molecule magnet bound together with neutral ligands, *Chem. Commun.*, 2020, **56**, 5677-5680.
97. S. Gupta, S. Dey, T. Rajeshkumar, G. Rajaraman and R. Murugavel, *ChemRxiv* 2021, DOI: 10.33774/chemrxiv-2021-h3qk7.
98. S. Corner, G. Gransbury, I. Vitorica-Yrezabal, G. Whitehead, N. Chilton and D. Mills, *ChemRxiv*, 2023, DOI: 10.26434/chemrxiv-2023-9l4wm.
99. Y. Liu, Y.-C. Chen, J. Liu, W.-B. Chen, G.-Z. Huang, S.-G. Wu, J. Wang, J.-L. Liu and M.-L. Tong, Cyanometallate-Bridged Didysprosium Single-Molecule Magnets Constructed with Single-Ion Magnet Building Block, *Inorg. Chem.*, 2020, **59**, 687-694.
100. S. Demir, M. I. Gonzalez, L. E. Darago, W. J. Evans and J. R. Long, Giant coercivity and high magnetic blocking temperatures for N_2^{3-} radical-bridged dilanthanide complexes upon ligand dissociation, *Nat. Commun.*, 2017, **8**, 2144-2144.
101. W. Cai, J. D. Bocarsly, A. Gomez, R. J. Letona Lee, A. Metta-Magaña, R. Seshadri and L. Echegoyen, High blocking temperatures for DyScS endohedral fullerene single-molecule magnets, *Chem. Sci.*, 2020, **11**, 13129-13136.

102. S. Demir, J. M. Zadrozny, M. Nippe and J. R. Long, Exchange Coupling and Magnetic Blocking in Bipyrimidyl Radical-Bridged Dilanthanide Complexes, *J. Am. Chem. Soc.*, 2012, **134**, 18546-18549.
103. N. Mavragani, D. Errulat, D. A. Gálico, A. A. Kitos, A. Mansikkamäki and M. Murugesu, Radical-Bridged Ln_4 Metallocene Complexes with Strong Magnetic Coupling and a Large Coercive Field, *Angew. Chem. Int. Ed.*, 2021, **60**, 24206-24213.
104. M. J. Giansiracusa, S. Al-Badran, A. K. Kostopoulos, G. F. S. Whitehead, D. Collison, F. Tuna, R. E. P. Winpenny and N. F. Chilton, A large barrier single-molecule magnet without magnetic memory, *Dalton Trans.*, 2019, **48**, 10795-10798.
105. S. Bala, G.-Z. Huang, Z.-Y. Ruan, S.-G. Wu, Y. Liu, L.-F. Wang, J.-L. Liu and M.-L. Tong, A square antiprism dysprosium single-ion magnet with an energy barrier over 900 K, *Chem. Commun.*, 2019, **55**, 9939-9942.
106. M. Fondo, J. Corredoira-Vázquez, A. M. García-Deibe, J. Sanmartín-Matalobos, S. Gómez-Coca, E. Ruiz and E. Colacio, Slow magnetic relaxation in dinuclear dysprosium and holmium phenoxide bridged complexes: a Dy_2 single molecule magnet with a high energy barrier, *Inorg. Chem. Front.*, 2021, **8**, 2532-2541.
107. X.-Q. Ji, J. Xiong, R. Sun, F. Ma, H.-L. Sun, Y.-Q. Zhang and S. Gao, Enhancing the magnetic performance of pyrazine-*N*-oxide bridged dysprosium chains through controlled variation of ligand coordination modes, *Dalton Trans.*, 2021, **50**, 7048-7055.
108. H. Wu, M. Li, Z. Xia, V. Montigaud, O. Cador, B. Le Guennic, H. Ke, W. Wang, G. Xie, S. Chen and S. Gao, High temperature quantum tunnelling of magnetization and thousand kelvin anisotropy barrier in a Dy_2 single-molecule magnet, *Chem. Commun.*, 2021, **57**, 371-374.
109. Z. Zhu, C. Zhao, Q. Zhou, S. Liu, X.-L. Li, A. Mansikkamäki and J. Tang, Air-Stable Dy(III)-Macrocycle Enantiomers: From Chiral to Polar Space Group, *CCS Chemistry*, 2022, **4**, 3762-3771.
110. X. L. Ding, Y. Q. Zhai, T. Han, W. P. Chen, Y. S. Ding and Y. Z. Zheng, A Local D_{4h} Symmetric Dysprosium(III) Single-Molecule Magnet with an Energy Barrier Exceeding 2000 K, *Chem. Eur. J.*, 2021, **27**, 2623-2627.
111. J. Xiong, H.-Y. Ding, Y.-S. Meng, C. Gao, X.-J. Zhang, Z.-S. Meng, Y.-Q. Zhang, W. Shi, B.-W. Wang and S. Gao, Hydroxide-bridged five-coordinate Dy(III) single-molecule magnet exhibiting the record thermal relaxation barrier of magnetization among lanthanide-only dimers, *Chem. Sci.*, 2017, **8**, 1288-1294.
112. P. B. Jin, Y. Q. Zhai, K. X. Yu, R. E. P. Winpenny and Y. Z. Zheng, Dysprosiacarboranes as Organometallic Single-Molecule Magnets, *Angew. Chem. Int. Ed.*, 2020, **59**, 9350-9354.
113. A. B. Canaj, S. Dey, O. Céspedes, C. Wilson, G. Rajaraman and M. Murrie, There is nothing wrong with being soft: using sulfur ligands to increase axiality in a Dy(iii) single-ion magnet, *Chem. Commun.*, 2020, **56**, 1533-1536.
114. K. L. M. Harriman, J. Murillo, E. A. Suturina, S. Fortier and M. Murugesu, Relaxation dynamics in see-saw shaped Dy(iii) single-molecule magnets, *Inorg. Chem. Front.*, 2020, **7**, 4805-4812.
115. S. Demir, M. D. Boshart, J. F. Corbey, D. H. Woen, M. I. Gonzalez, J. W. Ziller, K. R. Meihaus, J. R. Long and W. J. Evans, Slow Magnetic Relaxation in a Dysprosium Ammonia Metallocene Complex, *Inorg. Chem.*, 2017, **56**, 15049-15056.
116. Z.-H. Li, Y.-Q. Zhai, W.-P. Chen, Q.-C. Luo, T. Han and Y.-Z. Zheng, Breaking the axiality of pentagonal–bipyramidal dysprosium(iii) single-molecule magnets with pyrazolate ligands, *Inorg. Chem. Front.*, 2020, **7**, 4367-4376.
117. M. Li, H. Wu, Z. Xia, L. Ungur, D. Liu, L. F. Chibotaru, H. Ke, S. Chen and S. Gao, An Inconspicuous Six-Coordinate Neutral Dy^{III} Single-Ion Magnet with Remarkable Magnetic Anisotropy and Stability, *Inorg. Chem.*, 2020, **59**, 7158-7166.
118. J. Long, I. V. Basalov, N. V. Forosenko, K. A. Lyssenko, E. Mamontova, A. V. Cherkasov, M. Damjanović, L. F. Chibotaru, Y. Guari, J. Larionova and A. A. Trifonov, Dysprosium Single-Molecule Magnets with Bulky Schiff Base Ligands: Modification of the Slow Relaxation of the Magnetization by Substituent Change, *Chem. Eur. J.*, 2018, **25**, 474-478.
119. H.-M. Dong, H.-Y. Li, Y.-Q. Zhang, E.-C. Yang and X.-J. Zhao, Magnetic Relaxation Dynamics of a Centrosymmetric Dy_2 Single-Molecule Magnet Triggered by Magnetic-Site Dilution and External Magnetic Field, *Inorg. Chem.*, 2017, **56**, 5611-5622.
120. T. Han, W. Shi, Z. Niu, B. Na and P. Cheng, Magnetic Blocking from Exchange Interactions: Slow Relaxation of the Magnetization and Hysteresis Loop Observed in a Dysprosium-Nitronyl Nitroxide Chain Compound with an Antiferromagnetic Ground State, *Chem. Eur. J.*, 2012, **19**, 994-1001.
121. G. Lu, Y. Liu, W. Deng, G.-Z. Huang, Y.-C. Chen, J.-L. Liu, Z.-P. Ni, M. Giansiracusa, N. F. Chilton and M.-L. Tong, A perfect triangular dysprosium single-molecule magnet with virtually antiparallel Ising-like anisotropy, *Inorg. Chem. Front.*, 2020, **7**, 2941-2948.
122. S. Demir, M. Nippe, M. I. Gonzalez and J. R. Long, Exchange coupling and magnetic blocking in dilanthanide complexes bridged by the multi-electron redox-active ligand 2,3,5,6-tetra(2-pyridyl)pyrazine, *Chem. Sci.*, 2014, **5**, 4701-4711.
123. Z. H. Li, Y. Q. Zhai, W. P. Chen, Y. S. Ding and Y. Z. Zheng, Air-Stable Hexagonal Bipyramidal Dysprosium(III) Single-Ion Magnets with Nearly Perfect D_{6h} Local Symmetry, *Chem. Eur. J.*, 2019, **25**, 16219-16224.
124. S. Jia, X. Zhu, B. Yin, Y. Dong, A. Sun and D.-f. Li, Macrocyclic Hexagonal Bipyramidal Dy(III)-Based Single-Molecule Magnets with a D6h Symmetry, *Cryst. Growth Des.*, 2023, **23**, 6967-6973.
125. S.-S. Liu, Y.-S. Meng, Y.-Q. Zhang, Z.-S. Meng, K. Lang, Z.-L. Zhu, C.-F. Shang, B.-W. Wang and S. Gao, A Six-Coordinate Dysprosium Single-Ion Magnet with Trigonal-Prismatic Geometry, *Inorg. Chem.*, 2017, **56**, 7320-7323.
126. A. G. Bispo-Jr, L. Yeh, D. Errulat, D. A. Gálico, F. A. Sigoli and M. Murugesu, Improving the performance of β-diketonate-based Dy^{III} single-molecule magnets displaying luminescence thermometry, *Chem. Commun.*, 2023, **59**, 8723-8726.
127. J.-W. Yang, Y.-M. Tian, J. Tao, P. Chen, H.-F. Li, Y.-Q. Zhang, P.-F. Yan and W.-B. Sun, Modulation of the Coordination Environment around the Magnetic Easy Axis Leads to Significant Magnetic Relaxations in a Series of 3d-4f Schiff Complexes, *Inorg. Chem.*, 2018, **57**, 8065-8077.
128. G. Velkos, D. S. Krylov, K. Kirkpatrick, L. Spree, V. Dubrovin, B. Büchner, S. M. Avdoshenko, V. Bezmelnitsyn, S. Davis, P. Faust, J. Duchamp, H. C. Dorn and A. A. Popov, High Blocking Temperature of Magnetization and Giant Coercivity in the Azafullerene $Tb_2@C_{79}N$ with a Single-Electron Terbium-Terbium Bond, *Angew. Chem. Int. Ed.*, 2019, **58**, 5891-5896.

129. J. D. Rinehart, M. Fang, W. J. Evans and J. R. Long, A N_2^{3-} Radical-Bridged Terbium Complex Exhibiting Magnetic Hysteresis at 14 K, *J. Am. Chem. Soc.*, 2011, **133**, 14236-14239.
130. Z. Hu, H. Hu, Z. Chen, D. Liu, Y. Zhang, J. Sun, Y. Liang, D. Yao and F. Liang, Guest-Induced Switching of a Molecule-Based Magnet in a 3d–4f Heterometallic Cluster-Based Chain Structure, *Inorg. Chem.*, 2020, **60**, 633-641.
131. K. R. Meihaus and J. R. Long, Magnetic Blocking at 10 K and a Dipolar-Mediated Avalanche in Salts of the Bis(η^8-cyclooctatetraenide) Complex $[Er(COT)_2]^-$, *J. Am. Chem. Soc.*, 2013, **135**, 17952-17957.
132. A. P. Orlova, J. D. Hilgar, M. G. Bernbeck, M. Gembicky and J. D. Rinehart, Intuitive Control of Low-Energy Magnetic Excitations via Directed Dipolar Interactions in a Series of Er(III)-Based Complexes, *J. Am. Chem. Soc.*, 2022, **144**, 11316-11325.
133. X.-L.-. Ding, Y.-Q. Zhai, Q.-C. Luo and Y.-Z. Zheng, Chlorido-Bridged Didysprosium Single-Molecule Magnet Exhibiting 100-s Blocking Temperature near 8 K, *ChemRxiv*, 2021, DOI: doi:10.26434/chemrxiv-2021-ngqfl.
134. S. K. Langley, D. P. Wielechowski, V. Vieru, N. F. Chilton, B. Moubaraki, B. F. Abrahams, L. F. Chibotaru and K. S. Murray, A $\{Cr^{III}_2Dy^{III}_2\}$ Single-Molecule Magnet: Enhancing the Blocking Temperature through 3d Magnetic Exchange, *Angew. Chem. Int. Ed.*, 2013, **52**, 12014-12019.
135. B.-K. Ling, Y.-Q. Zhai, P.-B. Jin, H.-F. Ding, X.-F. Zhang, Y. Lv, Z. Fu, J. Deng, M. Schulze, W. Wernsdorfer and Y.-Z. Zheng, Suppression of zero-field quantum tunneling of magnetization by a fluorido bridge for a "very hard" 3d-4f single-molecule magnet, *Matter*, 2022, **5**, 3485-3498.
136. H. Kwon, K. R. McClain, J. G. C. Kragskow, J. K. Staab, M. Ozerov, K. R. Meihaus, B. G. Harvey, E. S. Choi, N. F. Chilton and J. R. Long, Coercive Fields Exceeding 30 T in the Mixed-Valence Single-Molecule Magnet $(CpiPr_5)_2Ho_2I_3$, *J. Am. Chem. Soc.*, 2024, **146**, 18714-18721.
137. J. M. Zadrozny, D. J. Xiao, M. Atanasov, G. J. Long, F. Grandjean, F. Neese and J. R. Long, Magnetic blocking in a linear iron(I) complex, *Nat. Chem.*, 2013, **5**, 577-581.
138. A. W. Cook, J. D. Bocarsly, R. A. Lewis, A. J. Touchton, S. Morochnik and T. W. Hayton, An iron ketimide single-molecule magnet $[Fe_4(N{=}CPh_2)_6]$ with suppressed through-barrier relaxation, *Chem. Sci.*, 2020, **11**, 4753-4757.
139. M. Heu, S. Yoon, B. J. Suh, D.-Y. Jung, J. W. Suk and Y. J. Kim, Magnetic Relaxation in a Single-Molecule Magnet Mn_{12}-chlorobutylate, *J. Kor. Phys. Soc.*, 2003, **43**, 544-547.
140. S. Verma, A. Verma, A. K. Srivastava, A. Gupta, S. P. Singh and P. Singh, Structural and magnetic properties of Mn_{12}-Stearate nanomagnets, *Mater. Chem. Phys.*, 2016, **177**, 140-146.
141. M. Laskowska, O. Pastukh, P. Konieczny, M. Dulski, M. Zalsiński and L. Laskowski, Magnetic Behaviour of Mn_{12}-Stearate Single-Molecule Magnets Immobilized on the Surface of 300 nm Spherical Silica Nanoparticles. *Materials*, 2020, **13**, 2624.
142. A. Verma, S. Verma, P. Singh and A. Gupta, Ageing effects on the magnetic properties of Mn_{12}-based Acetate and Stearate SMMs, *J. Magn. Magn. Mater.*, 2017, **439**, 76-81.
143. L. A. Kushch, V. D. Sasnovskaya, A. I. Dmitriev, E. B. Yagubskii, O. V. Koplak, L. V. Zorina and D. W. Boukhvalov, New single-molecule magnet based on Mn_{12} oxocarboxylate clusters with mixed carboxylate ligands, $[Mn_{12}O_{12}(CN\text{-}o\text{-}C_6H_4CO_2)_{12}(CH_3CO_2)_4(H_2O)_4]\cdot 8CH_2Cl_2$: Synthesis, crystal and electronic structure, magnetic properties, *Dalton Trans.*, 2012, **41**, 13747-13754.
144. D. Wu, D. Guo, Y. Song, W. Huang, C. Duan, Q. Meng and O. Sato, CoII Molecular Square with Single-Molecule Magnet Properties, *Inorg. Chem.*, 2009, **48**, 854-860.
145. S. K. Gupta, H. H. Nielsen, A. M. Thiel, E. A. Klahn, E. Feng, H. B. Cao, T. C. Hansen, E. Lelièvre-Berna, A. Gukasov, I. Kibalin, S. Dechert, S. Demeshko, J. Overgaard and F. Meyer, Multi-Technique Experimental Benchmarking of the Local Magnetic Anisotropy of a Cobalt(II) Single-Ion Magnet, *JACS Au*, 2023, **3**, 429-440.